

High Frequency Modeling of Current Sensors

J. Pankau D. Leggate D. Schlegel R. Kerkman G. Skibiniski

Rockwell Automation
Standard Drives Division
6400 W. Enterprise Drive Mequon, WI 53092
(414) 512-8263 (414) 512-8300 fax
rjkerkman@ra.rockwell.com

Abstract--Reflected wave transient voltages that result from fast Insulated Gate Bipolar Transistor voltage source inverters have received considerable investigation. Modeling, simulation, and attenuation of these transients require sophisticated motor and cable models. Most drive suppliers now provide combinations of passive and active solutions to mitigate the adverse effects of over voltage stress, however, the cost of the passive solutions often exceed the cost of the drive. Another aspect of low rise time devices, not examined to the extent of the over voltage problem, is the resulting current from traveling waves. Current sensor fidelity limits the ability of modern drives to detect peak current and can result in current feedback distortion. This paper presents recent research into the response, modeling, and construction of Hall effect current sensors. Models for Hall current sensors are introduced and compared. Experimental and simulation results demonstrate the complexity of the common current sensors employed in modern adjustable speed drives. A comparison of the sensor response and the model's prediction demonstrates the difficulty associated with accurate current detection. Finally, the paper presents design guidelines to reduce the corrupting influence of high frequency differential and common mode currents.

I. INTRODUCTION

Voltage Source Inverters (VSI) with 3rd generation Insulated Gate Bipolar Transistors (IGBT) dominate the low voltage adjustable speed industrial market. The fast rise times of 3rd generation IGBTs reduced the package size and in combination with high speed Digital Signal Processors provide performance characteristics comparable to dc drives. However, the fast rise times create significant problems such as motor over voltages, communications interference, and bearing currents [1-6].

As a result, the technical literature reflects an enormous effort investigating the undesirable characteristics of IGBTs on ac drive systems. System modeling, Pulse Width Modulation (PWM), and high frequency component modeling are all employed to understand and modify drive design to mitigate these effects. For example, the modeling of cables and the prediction of over voltages at the terminals of the motor has progressed from the simple 2 pu of an uncharged line to the complex interaction of cables and modulators to the > 2 pu of modern drive controllers. To accomplish this accuracy cable models have evolved from the simple loss-less line to more accurate cable modeling techniques encompassing cable construction types [7].

One consequence of the low-rise time voltages not examined in detail is the effect of the resulting high frequency inverter currents. A recent paper [8] was among the first to show the effects of high frequency currents – those due to reflected wave and parasitics – on current sensing, inverter control, and device operation. This paper presents simulation and experimental results demonstrating the effect of high frequency currents on current sensors. Models for the electronic and magnetic components of Hall effect sensors are included. Finally, recommendations for the sensor/feedback design and layout are presented which can improve feedback fidelity.

II. INVERTER PHASE CURRENTS: CHARACTERIZATION AND SENSING

A. Frequency Characterization: Experimental Results

Fig. 1 displays the *u*, *v*, and *w* phase to positive bus voltages and the *u*-phase current for a 460 Vrms, 10 hp motor operating no load at 40 Hz with an 8 kHz carrier. A 300 ft #12 AWG cable connected the inverter and motor. The current response shows a 300-400 kHz component, which is the cable oscillation frequency [6,8]. However, other high frequency components are present, which result from parasitic effects such as the inverter structure and motor.

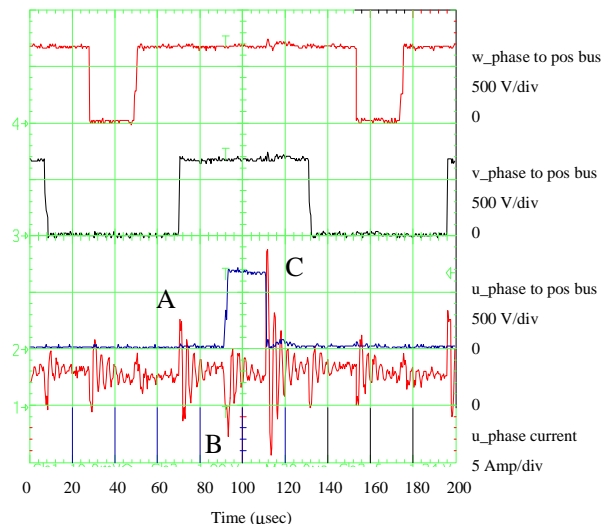


Fig. 1. Current disturbance during PWM pole switching at 300 ft of # 12 AWG cable.

Fig. 2 displays the phase current, current sensor output, and filtered output signal for the same induction motor as Fig. 1, however, with 10 ft of #12 AWG cable. The current exhibits a discernable 7.5 MHz component. The sensor amplifies this component and the filter transmits it unaffected. High frequencies, like the 7.5 MHz in Fig. 2, become dominant with shorter cable lengths [9]. The amplitude of the current is then determined by the parasitic impedance. Fig. 3 plots the impedance magnitude versus frequency for a 10 Hp induction motor, motor with 10 ft of #12 AWG cable, and motor with 300 ft of #12 AWG cable. Note the frequencies for the maximum and minimum impedances as the cable length changes.

One method for estimating the peak current is to establish the dominant frequency or frequencies based on the load and cable length. This frequency will be either the cable oscillation frequency (f_{oc}) or the first resonant minimum impedance frequency. Then the peak high frequency current is estimated by dividing the appropriate voltage by the corresponding impedance. For example consider 300 ft #12 AWG cable. The cable oscillation frequency is given by

$$f_{oc} = \frac{1}{4t_p} \quad (1)$$

t_p is the propagation delay, which is a function of cable type and length and in this case is 300-400 kHz [6,9]. The peak current associated with the forward traveling wave is approximately

$$i_{of} = \frac{V^+}{z_0} \quad (2)$$

V^+ is the forward voltage wave and z_0 is the cable surge impedance and for this example i_{of} is 8 amps peak. Finally, the dominant rise time frequency is given by

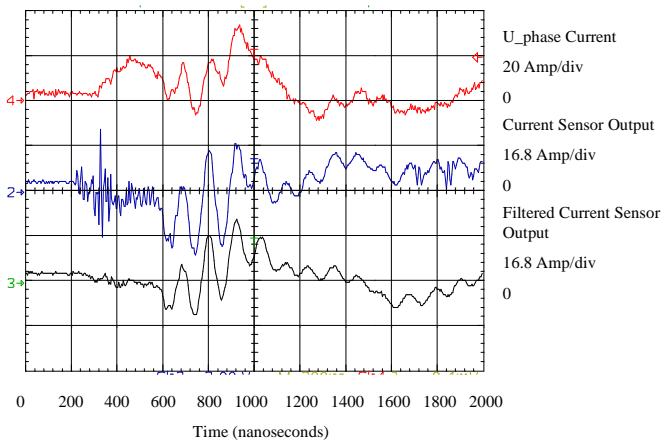


Fig. 2. Phase current, current sensor output, and filtered current sensor output at 10 ft of # 12 AWG cable.

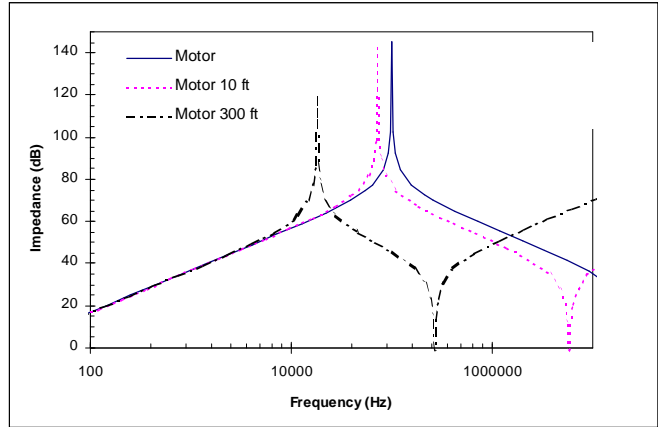


Fig. 3. Simulated system impedance relationships.

$$f_r = \frac{1}{\pi t_r} \quad (3)$$

t_r is the rise time of the power device. IGBTs with 50 nsec rise times yield a rise time frequency of 6.3 MHz. In this example, the peak current at this frequency is approximately 15 amps.

As the cable length increases, Fig. 3 shows the first differential mode impedance null slides left and theoretically aligns with the rise time frequency. In practice there exists a range of cable lengths for which the impedance is low enough to excite a resonance with excessive peak current. At these frequencies current sensing is unreliable, interference with surrounding circuitry and sensors intolerable, and unsafe operation of equipment is possible. Therefore, accurate monitoring of drive current and quantifying the limitations of the sensors is necessary to ensure reliability.

B. Current Sensing

Fig. 4 shows a typical current feedback arrangement. The sensor and passive RC are located on the power driver board. A feedback signal is brought to the control board through a

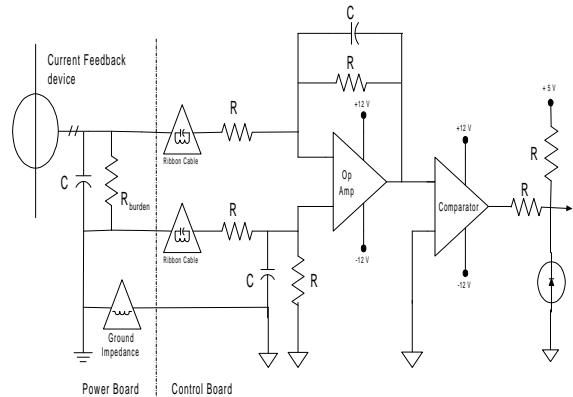


Fig. 4. Typical current feedback circuit arrangement.

ribbon cable. The cable has insertion impedance and cross talk characteristics. The power board ground is differentiated from control board ground to account for the effects of high frequency currents. Recent literature has demonstrated substantial high frequency current – both differential and common mode – on multiple motor and common bus applications [10]. This is important for determining the effectiveness of the low pass or anti-aliasing filter of Fig. 4. Finally, the low pass signal is A/D and/or fed to the current polarity detector.

A particular current sensor’s fidelity depends on the frequency content of the sensed signal. Figs. 5 and 6 show signals at different time sweeps. Fig. 5 displays the line to positive bus voltage at the inverter output, motor phase current, current feedback, and a current polarity signal for an inverter with 50 ns rise time and 600 ft of #12 AWG cable. At the instant of switching, the current feedback signal exhibits high frequency corruption for approximately 600 ns, followed by an under-damped distortion at 3 times the cable oscillation frequency. Simultaneously, the polarity detector reacts to the current feedback signal, but clearly contributing its own distortion and misrepresentation of the current feedback’s polarity. Often the polarity detector incorporates hysteresis or a rate limit. However, this can result in desensitizing protection circuitry and delayed polarity detection.

Fig. 6 shows the *u* phase upper and lower inverter voltages, *u*-phase current, and the *u* phase dead time polarity detector. Notice the high frequency coupling in the *u*-phase current. Of more interest is the false switching of the polarity detector resulting from common mode corruption of the current feedback signal.

III. CURRENT SENSOR MODELING

Fig. 7 shows a functional model of a closed-loop Hall effect current sensor. Primary current (I_p) flowing through the conductor produces a magnetic field. The flux produced is

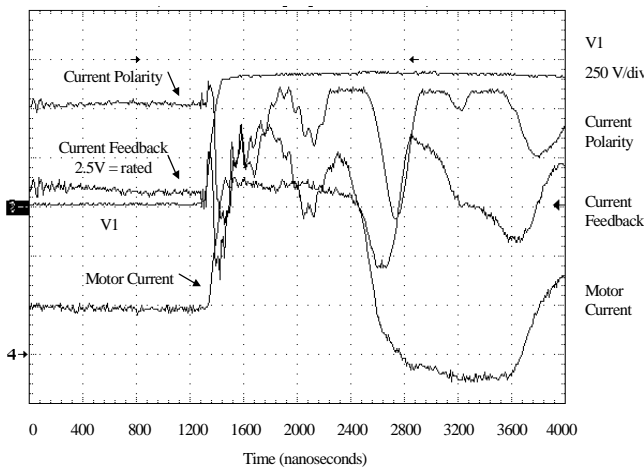


Fig. 5. Experimental results with current feedback signal distortion.

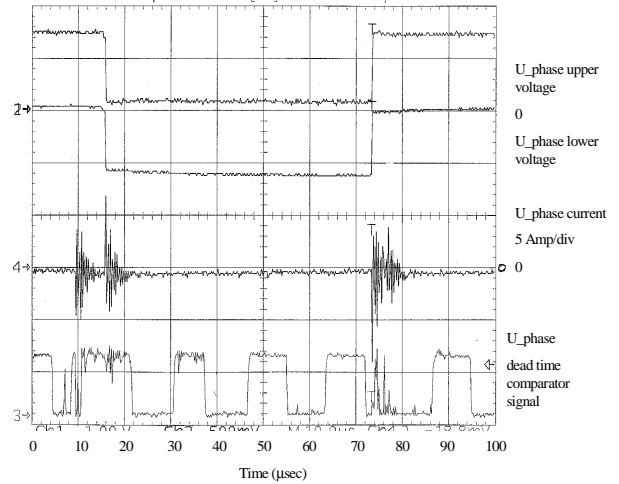


Fig. 6. Experimental results with dead time current polarity distortion.

concentrated in the core and is proportional to I_p . A Hall device in the air gap produces a voltage proportional to the flux density, B_x , in the core. The Hall voltage is amplified by an op-amp, then fed to a push-pull amplifier. The push-pull amplifier drives the secondary winding on the core, which is wound in series opposition to null the flux in the core. Operating the core near zero flux eliminates the dependence on the linearity of the core and Hall device and also reduces hysteresis errors. The secondary current (I_s) can be converted to a voltage by placing a resistor from the output of the secondary coil to ground. A capacitor is often added to attenuate high frequencies. By selecting the proper resistor/capacitor values, the voltage can be scaled for any application.

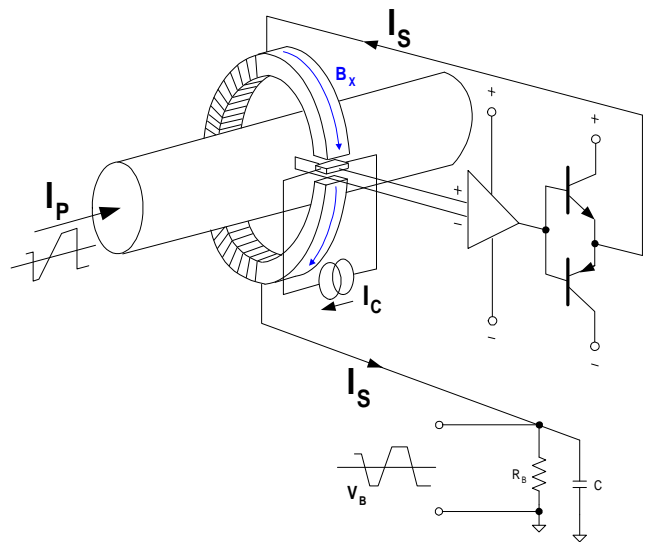


Fig. 7. Closed-loop Hall effect current sensor diagram [7,11].

A. Second Order Current Sensor Model

Fig. 8 presents a simple model for the sensor. Here the motor phase current serves as a current source. The sensor is subdivided into a magnetic component (single phase transformer), a control component (Proportional/Integral $K_p K_i$), and a load component (parallel r_b and C). The transfer function of the sensor is given by

$$\frac{V_B}{I_p} = \frac{s a_1 + a_0}{s^2 b_2 + s b_1 + b_0} \quad (4)$$

where

$$\begin{aligned} a_0 &= -r_b L_m K_i, a_1 = -r_b L_m (K_p - 1), b_0 = r_b C (K_p L_m - L_{22}) \\ b_1 &= (-r_2 r_b C + L_m K_i r_b C - L_{22} + K_p L_m), b_2 = -r_b + L_m K_i - r_2 \end{aligned} \quad (5)$$

Data necessary to establish K_p and K_i were obtained from the manufacturer for a range of sensor ratings. The results reported in this paper are for a 25 ampere device. Tests were performed on the magnetic core to obtain the equivalent transformer parameters. The results of these tests and the controller gains are listed in Table I. The above transfer function is plotted in Fig. 9 together with the frequency response of the sensor. The low frequency response is in good agreement with the manufacturers published specifications [11]. Notice the model's high frequency characteristics require a more complex model.

Modern drives employing 3rd generation IGBTs require fast over current protection and accurate current sampling for control purposes. The current sensor response shown in Fig. 9, however, presents significant design problems. Over current protection requires detecting peak current. "Noisy" feedback current often requires desensitizing the protection circuitry to prevent nuisance over current trips. In addition,

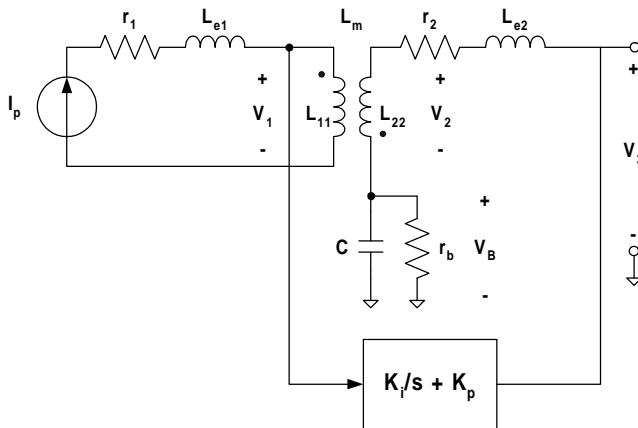


Fig. 8. Simple model for current sensor.

TABLE I

Control Gains and Magnetic Circuit Parameters for Simple Sensor Model

K_i	K_p	K_{Hall_eff}	r_2	L_{22}	L_m	r_b	C
10^6	10^3	8 V/Wb	100 Ω	169.1 mH	169 mH	169 Ω	8200 pF

when used for control the current feedback is often sampled at a zero vector to provide a theoretically optimal value of the fundamental component. Furthermore, an undistorted polarity detection makes dead time compensation extremely accurate. Fig. 9, however, shows the high frequency components are amplified by the transducer; thus the effectiveness of the dead time compensation and a current loop's bandwidth can be reduced.

With this background, a review of Figs. 2 and 5 is instructive. A 50 ns rise time has a characteristic harmonic of 6.3 Mhz. The cable provides a 300-400 kHz cable oscillation frequency. From Fig. 9 the sensor attenuates the cable oscillation frequency. However, the 6.3 MHz component associated with the IGBT rise time is amplified by the sensor and it along with the high frequency motor currents create a highly distorted feedback signal.

In summary, the phase current spectrum is a function of power device rise time, cable type and cable length, and motor. The dominant frequencies are determined by the relative impedance magnitude of the cable and motor. Finally, the high frequency amplification by the sensor and associated ground bounce can present signals with bandwidths beyond the design range of detection and protection circuitry.

B. Sensor Model Employing Control Component and Magnetic Analysis

With feedback circuitry designed to provide high resolution of the fundamental component, the additional high

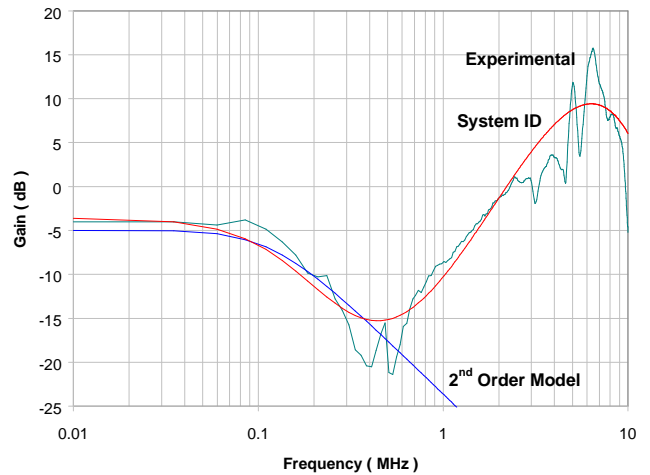


Fig. 9. Current transducer bandwidth and system ID.

frequency di/dt induced by the low rise time IGBT and load can result in conditions exceeding the sensor's specifications. An investigation of the dynamic performance of current sensor for purposes of evaluation and design requires models that are more complete than the 2nd order model above. A more accurate sensor model may be developed by dividing the sensor into two major components – control circuit and magnetics.

Fig. 10 shows the Hall sensor, control hardware, and transformer. Physically, the Hall device is centered in the air gap of the transformer. Fig. 10 depicts this by coupling the transformer flux density, B_x , as an input to the Hall sensor. Fig. 11 shows the equivalent magnetic circuit and relevant equations used in modeling the sensor's transformer. Fig. 12 displays the B-H characteristics for the 25 amp sensor and is representative of core material in Hall based current sensors. Employing the equations associated with the magnetic circuit of Fig. 11, the control winding inductance was determined to be 169 mH, which is identical to that obtained above using an LCR meter.

A similar procedure may be applied to the control electronics. When combined with the model for the magnetic core, a more complete sensor model results, which is easily combined with machine, cable, and inverter models in a SIMULINK package [12,13].

C. Sensor Model Employing System Identification

Even though the sensor model presented above incorporates saturation of the core and detail of the control electronics, the high frequency characteristics are not modeled. System identification procedures may be used to improve the high frequency representation for simulation studies and assist in board layout and design. Many software packages exist to fit functions – polynomials or exponentials for example – to test data. The model given by (6) was obtained from MATHCAD

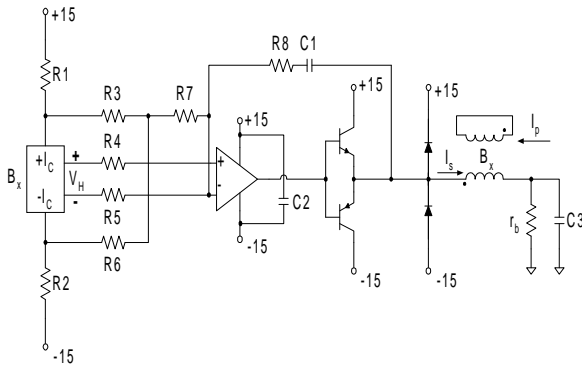
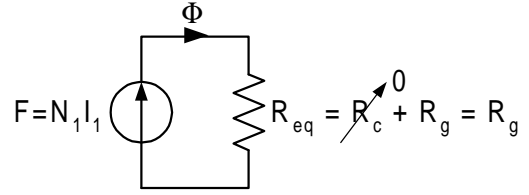


Fig. 10. Magnetic core, Hall sensor, control winding and equivalent magnetic circuit.



$$\lambda_2 = N_2 \phi = NAB \quad L_{22} = \frac{N_2^2}{R_{eq}}$$

$$L_{21} = \frac{\lambda_2}{I_1} \quad H = \frac{N_1 I_1}{l_g}$$

Fig. 11. Magnetic equivalent circuit.

genfit equation routine [14]. (6) is easily interfaced with the SIMULINK simulation blocks for the inverter, cable, and motor. The model's frequency response is plotted in Fig. 9.

$$\frac{V_B}{I_s} = 9 \times 10^{64} \frac{(s + 2.6 \times 10^6)^5}{(s + 10^6)^3 (s + 8 \times 10^7)^{10}} \quad (6)$$

IV. EXPERIMENTAL AND SIMULATION RESULTS

In an earlier paper [8], the authors showed the effects of the currents' high frequency components on current sensing and commutation of the inverter. Of the many factors contributing to the degradation of feedback fidelity, those

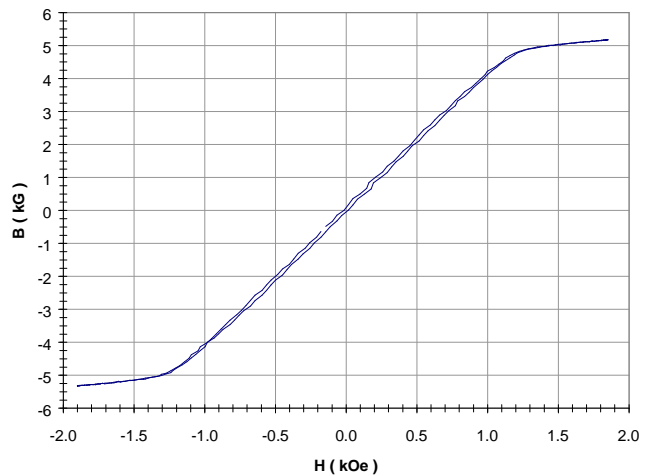


Fig. 12. B-H curve of current sensor magnetic core.

associated with the power and control board layout are difficult to identify and minimize. A test fixture with the sensors under test powered by isolated linear amplifiers reduces the effects of power supply harmonics, phase to phase interference, signal cross talk and provides simultaneous comparison of sensor technology.

Tests were conducted on three current sensors: a Hall sensor located on an IGBT power board, a Hall sensor with a Faraday shield, and a magnetoresistive sensor. All sensors were measuring the same phase current. The rise time of the inverter was 50 nsec. The inverter was connected to a 10 hp induction motor by a 310 ft #12 AWG cable and the carrier was 4 kHz. The results of the test are displayed in Fig. 13.

The cable oscillation frequency is approximately 316 kHz, which is clearly present in the phase current. It is important to note the peak current associated with this component. Peak currents in excess of drive rating are often observed. The amplitude of this component is determined by the cable's characteristic impedance. The phase current's transient response over the initial 2 μ sec also exhibits a 5-6 MHz component. Although damped, this component excites all three current sensors, the peak determined by the transducer's transfer characteristic. A prominent under damped 632 kHz component is evident in the control board sensor's signal. Neither the shielded Hall or magnetoresistive sensor exhibited this component. Possible sources for the distortion are power supply corruption and saturation of the sensor core.

Fig. 14 displays simulation results for the more complete sensor models. Fig. 14a shows the inverter voltage, motor terminal voltage, and phase current. Fig. 14b demonstrates details of the magnetic model. The core flux linkages (Λ), secondary current (I_2) and push pull voltage

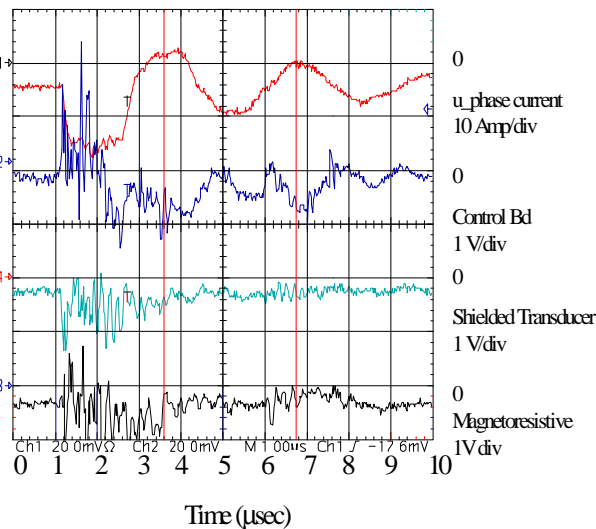


Fig. 13. Current feedback transducer fidelity.

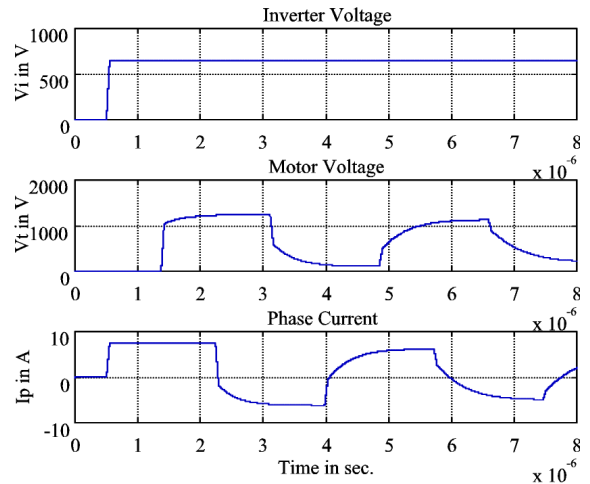


Fig. 14a. Sensor model simulation results: Inverter voltage, motor terminal voltage, and phase current.

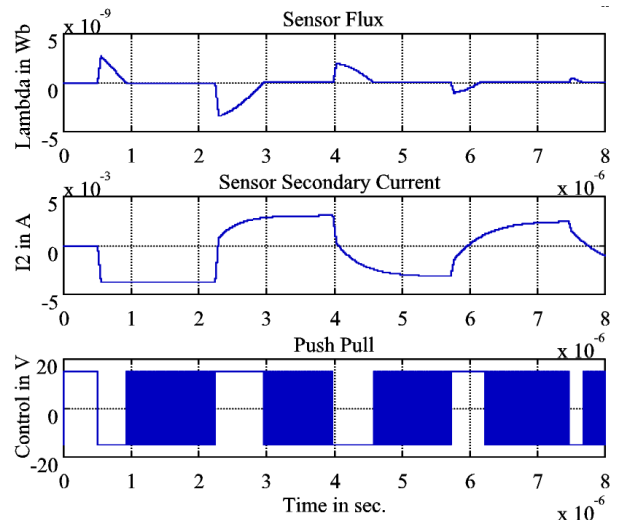


Fig. 14b. Sensor model simulation results: Details of magnetic model.

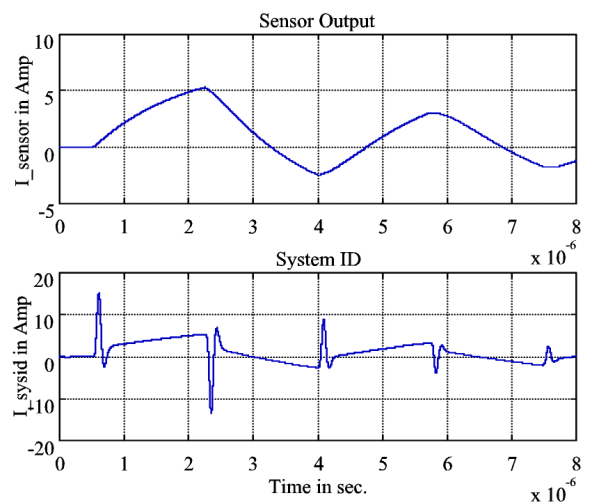


Fig. 14c. Sensor model simulation results: Sensor feedback signals for magnetic and system identification models.

(Control) are displayed. Note the dynamic response of the core's flux linkages. The peak flux linkages is well below the saturation value (3×10^{-7} Wb turns). The cable oscillation frequency periodically disturbs the null condition of the core, which drives the PI output and momentarily saturates the push-pull amplifier. The ability of the control circuitry to null the core is severely taxed when the dwell time between PWM pulses becomes less than the relaxation time of the sensor [6].

Fig. 14c compares sensor feedback signals for the magnetic and system identification models. While the magnetic model accurately attenuates the cable oscillation frequency, it fails to predict the 6 MHz component. This is consistent with the bandwidth for this model as displayed in Fig. 9. The system identification model reproduces the 6 MHz spikes corresponding to the motor, which are evident in Fig 2 and to a lesser extent in Fig's. 5 and 13.

V. SUMMARY AND RECOMMENDATIONS

A. Summary

The following summarizes the research on Hall effect sensors:

- Sensor model complexity is dependent on the bandwidth of interest.
- System modeling techniques provide accurate high frequency model for analysis and simulations.
- Modern drives have di/dt which can exceed the di/dt rating of Hall effect sensors.
- Response time of sensor is greater than the rise time of the current.
- Frequency content of phase current excites the undesirable region of the sensor.
- Sensor electronic components are specified within expected frequency range.
- Ground, power supply integrity, and anti-aliasing filter effectiveness are dependent on power/control board layout and inter-ground impedance.
- Shielded sensors reduce interference and improve signal fidelity for control purposes.

B. Recommendations

- Employ shielded sensors to maximize fundamental component fidelity for zero vector sampling.
- Employing high sampling rate A/D converters and averaging principles in lieu of zero vector sampling can mitigate the undesirable characteristics of the sensor.
- Sampling rates must be based on the expected cable oscillation and rise time frequencies to prevent aliasing.

VI. CONCLUSIONS

High frequency currents produced by 3rd generation IGBTs in combination with load parasitics were presented in the paper. The effects of cables, cable lengths, and motors on the current's high frequency content were identified and their interaction displayed through appropriate component models. Hall effect current sensors and sensor feedback circuitry were investigated and modeled. Bode plots of the sensor transfer function were used to refine the sensor models. The sensor models allow for investigations of second order effects - sensor saturation, eddy currents, power supply distortion - on current fidelity. Finally, the paper presented recommendations for sensor/feedback design and layout to improve current sensor fidelity.

REFERENCES

- [1] S. Evon, D. Kempke, L. Saunders, and G. Skibinski, "Riding the reflected wave - IGBT drive technology demands new motor and cable considerations," 1996 IEEE Petroleum and Chemical Industry Conference, Philadelphia PA, Sept. 23-27, 1996, pp. 75-84.
- [2] E. Persson, "Transient effects in application of PWM inverters to induction motors," IEEE IAS Transactions, Vol. 28. No. 5, Sept./Oct. 1992, p.1095.
- [3] P. Van Paucke, R. Belmans, W. Geysen, and E. Ternier, "Overvoltages in inverter fed induction machines using high frequency power electronic components," IEEE APEC Conference Proceeding, March 1994, pp. 536-541.
- [4] T. Takahashi, M. Termeyer, T. Lowery, and H. Tsai, "Motor lead length issues for IGBT drives," 1995 IEEE Pulp and Paper Conference, pp. 21-27.
- [5] G. Skibinski, J. Erdman, J. Pankau, J. Campbell, "Assessing ac motor dielectric withstand capability to reflected voltage stress using corona testing," IEEE IAS Conference Record, San Diego, CA, Oct. 6-10, 1996, pp. 694-702.
- [6] R. Kerkman, D. Leggate, G. Skibinski, "Interaction of drive modulation & cable parameters on ac motor transients," IEEE IAS Conference Record, San Diego, CA, Oct. 6-10, 1996, pp. 143-152.
- [7] G. Skibinski, R. Kerkman, D. Leggate, J. Pankau, and D. Schlegel "Reflected wave modeling techniques for PWM AC motor drives", APEC Conference Proceedings, Anaheim, CA, Feb. 1998, pp. 1021-1029.
- [8] D. Leggate, J. Pankau, D. Schlegel, R. Kerkman, and G. Skibinski, "Reflected wave and their associated currents", IEEE IAS Conference Record, St Louis, MO, Oct. 1998, pp. 789-798.
- [9] G. Skibinski, R. J. Kerkman, D. Leggate, "Cable characteristics and their influence on motor over-voltages," IEEE APEC Conference Proceedings, Atlanta, GA, Feb. 23-27, 1997, pp. 114-121.
- [10] G. Skibinski, D. Dahl, K. Pierce, R. Freed, and D. Gilbert, "Installation considerations for multi-motor AC drives & filters used in metal industry applications," IEEE Conference Record, St. Louis, MO, Oct. 1998, pp. 2270-2278.
- [11] LEM USA, Inc., Technical File, June 8, 1998.
- [12] Chee-Mun Ong, *Dynamic Simulation of Electric Machinery: Using Matlab/Simulink*, Prentice Hall PTR, Upper Saddle River, NJ
- [13] SIMULINK with MATLAB, The MathWorks, Inc.
- [14] Mathcad, Mathsoft, Inc., Version 7.0.